

ARTICLE

<https://doi.org/10.1038/s41467-019-12843-w>

OPEN

# Atomically dispersed nickel as coke-resistant active sites for methane dry reforming

Mohcin Akri<sup>1,12</sup>, Shu Zhao<sup>2,12</sup>, Xiaoyu Li<sup>1,3</sup>, Ketao Zang<sup>4</sup>, Adam F. Lee<sup>5</sup>, Mark A. Isaacs<sup>6</sup>, Wei Xi<sup>4</sup>, Yuvaraj Gangarajula<sup>1</sup>, Jun Luo<sup>4</sup>, Yujing Ren<sup>1</sup>, Yi-Tao Cui<sup>7</sup>, Lei Li<sup>8</sup>, Yang Su<sup>1</sup>, Xiaoli Pan<sup>1</sup>, Wu Wen<sup>9</sup>, Yang Pan<sup>9</sup>, Karen Wilson<sup>5</sup>, Lin Li<sup>1</sup>, Botao Qiao<sup>1,10\*</sup>, Hirofumi Ishii<sup>11</sup>, Yen-Fa Liao<sup>11</sup>, Aiqin Wang<sup>1</sup>, Xiaodong Wang<sup>1</sup> & Tao Zhang<sup>1,3\*</sup>

Dry reforming of methane (DRM) is an attractive route to utilize CO<sub>2</sub> as a chemical feedstock with which to convert CH<sub>4</sub> into valuable syngas and simultaneously mitigate both greenhouse gases. Ni-based DRM catalysts are promising due to their high activity and low cost, but suffer from poor stability due to coke formation which has hindered their commercialization. Herein, we report that atomically dispersed Ni single atoms, stabilized by interaction with Ce-doped hydroxyapatite, are highly active and coke-resistant catalytic sites for DRM. Experimental and computational studies reveal that isolated Ni atoms are intrinsically coke-resistant due to their unique ability to only activate the first C-H bond in CH<sub>4</sub>, thus avoiding methane deep decomposition into carbon. This discovery offers new opportunities to develop large-scale DRM processes using earth abundant catalysts.

<sup>1</sup>CAS Key Laboratory of Science and Technology on Applied Catalysis, Dalian Institute of Chemical Physics, Chinese Academy Sciences, 116023 Dalian, China. <sup>2</sup>Beijing Guyue New Materials Research Institute, Beijing University of Technology, 100124 Beijing, China. <sup>3</sup>University of Chinese Academy of Sciences, 100049 Beijing, China. <sup>4</sup>Center for Electron Microscopy and Tianjin Key Lab of Advanced Functional Porous Materials, Institute for New Energy Materials, School of Materials Science and Engineering, Tianjin University of Technology, 300384 Tianjin, China. <sup>5</sup>Applied Chemistry & Environmental Science, RMIT University, Melbourne 3000, Australia. <sup>6</sup>Department of Chemistry, University College London, London, UK. <sup>7</sup>Synchrotron Radiation Laboratory, Laser and Synchrotron Research Center (LASOR), The Institute for Solid State Physics, The University of Tokyo, 1-490-2 Kouto, Shingu-cho Tatsuno, Hyogo 679-5165, Japan. <sup>8</sup>Synchrotron Radiation Research Center, Hyogo Science and Technology Association, Hyogo 679-5165, Japan. <sup>9</sup>National Synchrotron Radiation Laboratory, University of Science and Technology of China, Hefei 230029, China. <sup>10</sup>Dalian National Laboratory for Clean Energy, 116023 Dalian, China. <sup>11</sup>National Synchrotron Radiation Research Center, Hsinchu 30076, Taiwan (ROC). <sup>12</sup>These authors contributed equally: Mohcin Akri and Shu Zhao. \*email: [bqiao@dicp.ac.cn](mailto:bqiao@dicp.ac.cn); [taozhang@dicp.ac.cn](mailto:taozhang@dicp.ac.cn)

**D**ry reforming of methane (DRM) is the process of converting methane ( $\text{CH}_4$ ) and carbon dioxide ( $\text{CO}_2$ ) into synthesis gas (syngas,  $\text{H}_2 + \text{CO}$ )<sup>1–3</sup>, an important building block for world scale industrial processes and energy conversion such as Fischer-Tropsch (FT), carbonylation, hydroformylation, and for the syntheses of fuels and high value-added chemicals<sup>3–6</sup>.  $\text{CO}_2$  and  $\text{CH}_4$  are the two most important atmospheric greenhouse gases (GHGs) responsible for anthropogenic climate change<sup>7</sup>, but are also abundant and low-cost carbon sources<sup>8</sup>; the latter is regarded as a (relatively) clean energy source with which to realize a low-carbon economy<sup>9</sup>. Despite the emergence of DRM around 30 years ago<sup>10</sup>, its potential to mitigate rising GHG emissions and provide clean(er) fossil fuel utilization has sparked renewed interest in associated catalytic technologies<sup>2,11–16</sup>.

Almost 30 years' of intensive studies have identified Ni catalysts as the most promising candidate for DRM due to their low cost and high initial activity (comparable to noble metal catalysts)<sup>1,2,12,17</sup>. However, there are no commercial DRM processes to date due in large part to in situ catalyst deactivation by carbon deposition (coking) and/or sintering of Ni species<sup>12,18</sup>. Previous studies have shown that support acidity<sup>17,19</sup> and the dimensions of catalytically active components strongly influence carbon deposition<sup>12,20</sup>. Several studies have identified a threshold Ni nanoparticle size (2 nm<sup>21</sup> or 7–10 nm<sup>22</sup>) below which the carbon deposition significantly decreases. However, small Ni particles generally exhibit poor thermal stability and are prone to sintering under DRM reaction conditions, presenting an intractable problem.

Single-atom catalysts (SACs) comprising isolated, individual metal atoms dispersed on a solid support, have recently emerged as a new frontier in catalysis and materials science<sup>23–29</sup>. Although generally considered thermodynamically unstable, recent studies have revealed instances wherein atomically dispersed metals can actually be much more thermally stable and durable than their nanocatalyst counterparts<sup>30–34</sup>. Considering that Ni atoms in SACs are certainly below the threshold size to be coke-resistant in DRM, well-designed stable Ni SACs should be an ideal candidate for DRM provided that they are sufficiently active. Herein, we demonstrate that Ni atomically dispersed over hydroxyapatite (HAP) is highly active and completely coke-resistant during high temperature DRM.  $\text{CeO}_x$  doping of HAP traps isolated Ni atoms, preventing on-stream sintering and deactivation and resulting in an active and stable high-performance DRM catalyst. This finding provides a new route for the development of coke-resistant DRM catalysts.

## Results

**Structural characterization of Ni single-atom catalyst.** HAP and Ce-substituted HAP with a Ce metal loading of 5 wt% (denoted as HAP-Ce) were prepared by a previously reported co-precipitation (CP) method<sup>35</sup>. Ni atoms were subsequently deposited over the HAP support with a nominal loading of 0.5 wt% (denoted as 0.5Ni<sub>1</sub>/HAP), and the HAP-Ce support with loadings of 0.5 wt%, 1 wt%, and 2 wt% (denoted as 0.5Ni<sub>1</sub>/HAP-Ce, 1Ni<sub>1</sub>/HAP-Ce, and 2Ni<sub>1</sub>/HAP-Ce), by strong electrostatic adsorption (SEA)<sup>30,36,37</sup>. For comparison, Ni nanocatalysts with 10 wt% loading were prepared by the same method over HAP and HAP-Ce supports, denoted as 10Ni/HAP and 10Ni/HAP-Ce, respectively. Synthesis details are provided in the Methods section.

Actual Ni metal loadings of the as-prepared catalysts were determined by inductively coupled plasma atomic emission spectroscopy (ICP-AES), and were similar to the nominal values (Supplementary Table 1) except for 10Ni/HAP-Ce which

contained 8.5 wt% Ni. Textural properties of Ce-doped HAP were similar to the undoped support (Supplementary Fig. 1a and Supplementary Table. 2). However,  $\text{CO}_2$  temperature-programed desorption (TPD, Supplementary Fig. 1b) showed that ceria addition decreased the density of both weak and strong base sites, indicating that  $\text{CeO}_x$  is less basic than HAP.

The X-ray diffraction (XRD) pattern of HAP-Ce evidenced no crystalline  $\text{CeO}_2$  phases (Supplementary Fig. 2a), suggesting that cerium is either highly dispersed on the HAP external surface or doped into the lattice. Ni and NiO reflections were also absent from all unreduced samples (Supplementary Fig. 2b), suggesting that Ni/NiO were highly dispersed on both supports even following high temperature calcination (500 °C). For samples subsequently reduced under  $\text{H}_2$  at 500 °C, only 10 wt% Ni samples show reflections characteristic of fcc nickel metal at 44.6° (Supplementary Fig. 2c, indicated by arrows). Corresponding Ni particle sizes were calculated according to the Scherrer equation as 17.0 and 10.6 nm for 10Ni/HAP and 10Ni/HAP-Ce, respectively, suggesting the introduction of Ce inhibited the sintering of Ni nanoparticles. For 0.5 wt% loadings, the absence of crystalline Ni and/or NiO phases may reflect the formation of highly dispersed Ni species, or instrumental detection limit due to the low Ni loading. All samples were therefore examined by (aberration corrected) high-angle annular dark-field scanning transmission electron microscopy (ac-HAADF-STEM) to identify the nature of supported Ni species. Neither Ni nanoparticles nor clusters were visible in relatively low magnification images for as-prepared 0.5Ni<sub>1</sub>/HAP and 0.5Ni<sub>1</sub>/HAP-Ce samples (Supplementary Fig. 3a, b), whereas higher magnification images (Supplementary Fig. 3c, d) clearly revealed the exclusive presence of isolated Ni atoms, confirming 0.5Ni<sub>1</sub>/HAP and 0.5Ni<sub>1</sub>/HAP-Ce as SACs before reduction. Following 500 °C  $\text{H}_2$  reduction the 0.5Ni<sub>1</sub>/HAP-Ce sample still predominantly comprised atomically dispersed Ni (Fig. 1a and Supplementary Fig. 4), in addition to a small number (~7% frequency, Fig. 1d) of sub-1.5 nm Ni clusters. For 1Ni<sub>1</sub>/HAP-Ce and 2Ni<sub>1</sub>/HAP-Ce catalysts, low magnification images (Supplementary Figs. 5 and 6) showed the presence of a low density of ~1 nm nanoclusters, indicating that nickel predominantly existed as single atoms (Fig. 1b–d). In contrast, the as-prepared, 10 wt% samples comprised small (~1–2 nm) NiO clusters/nanoparticles over both supports (Supplementary Fig. 7a, b), which grew post-reduction to generate a distribution of small (1–3 nm) and large (5–10 nm) nanoparticles for 10Ni/HAP-Ce (Fig. 1c and Supplementary Fig. 7c) and a broad nanoparticle distribution (2–17 nm) for 10Ni/HAP (Supplementary Fig. 7d) in accordance with XRD.

The coordination environment of Ni atoms was further determined by quasi in situ X-ray absorption spectroscopy (XAS) measurements. Ni K-edge X-ray near-edge absorption spectra (XANES) collected after 500 °C reduction show that 2Ni<sub>1</sub>/HAP-Ce possessed an intense white line reminiscent of NiO (Fig. 2a), whereas 10Ni/HAP-Ce exhibited a weaker white line and strong pre-edge feature more closely resembling Ni foil, characteristic of oxidized and metallic chemical states respectively. Corresponding extended X-ray absorption fine structure (EXAFS) spectra confirmed the dominant presence of Ni-Ni scattering distances at ~2.50 Å (Fig. 2b) for 10Ni/HAP-Ce. In contrast, 2Ni<sub>1</sub>/HAP-Ce exhibited strong Ni-O scattering at 2.05 Å, a significant 2.60 Å contribution attributed to Ni-Ce scattering, and only a weak Ni-Ni contribution (corresponding to a coordination number ~0.7); these observations are consistent with atomically dispersed Ni (Supplementary Table 3 and Supplementary Fig. 8). XAS data are thus in good agreement with AC-HAADF-STEM imaging (Fig. 1b).

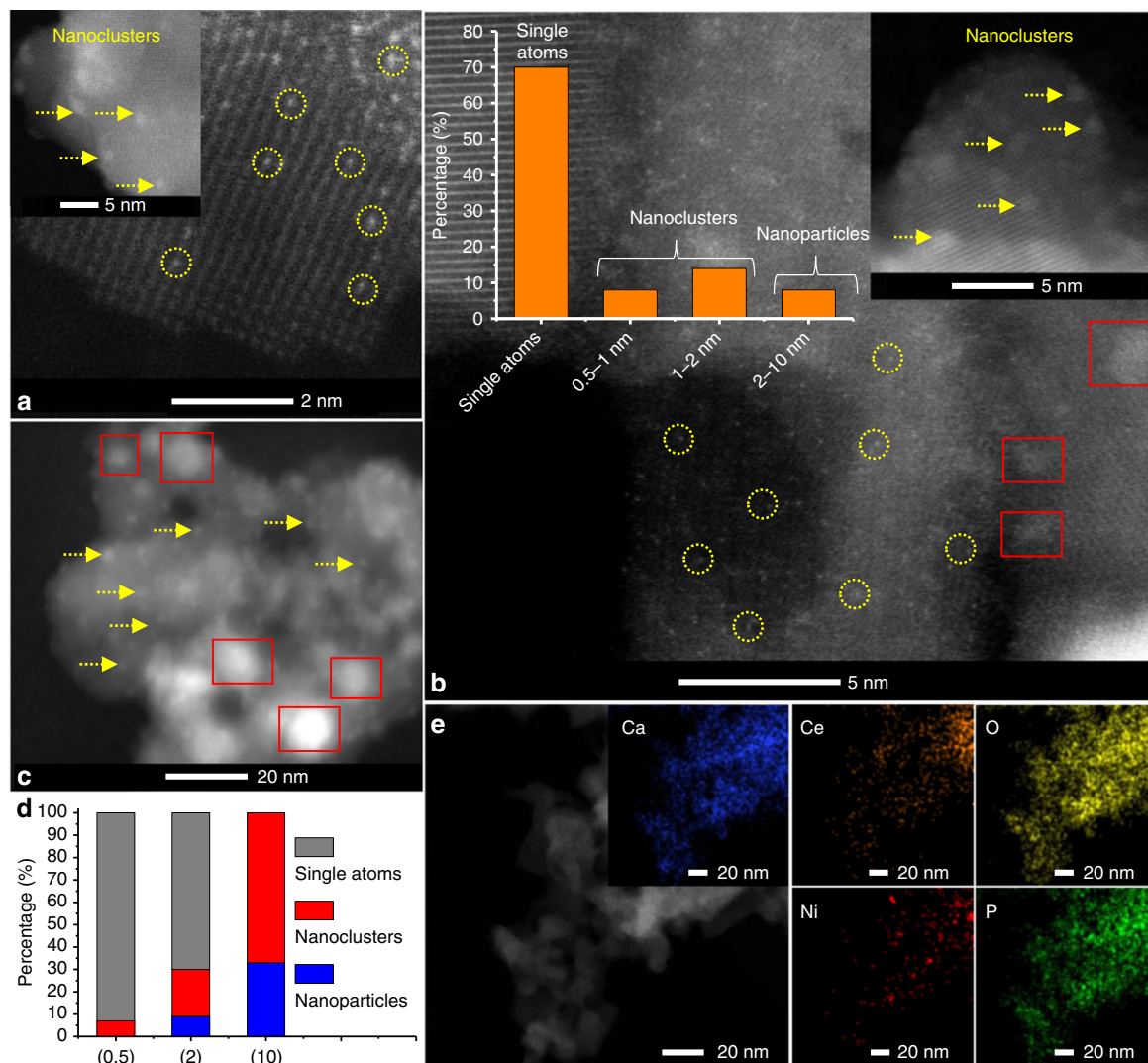


**Fig. 1** Electron microscopy images and size distribution of Ni/HAP-Ce samples. **a** HAADF-STEM images of 0.5Ni<sub>1</sub>/HAP-Ce, **b** 2Ni<sub>1</sub>/HAP-Ce, and **c** 10Ni<sub>1</sub>/HAP-Ce samples after 500 °C H<sub>2</sub> reduction. **d** particle size distributions of **a-c**; yellow circles indicate atomically dispersed Ni and red squares indicate Ni metals nanoparticles. **e** EDX element maps of 0.5Ni<sub>1</sub>/HAP-Ce

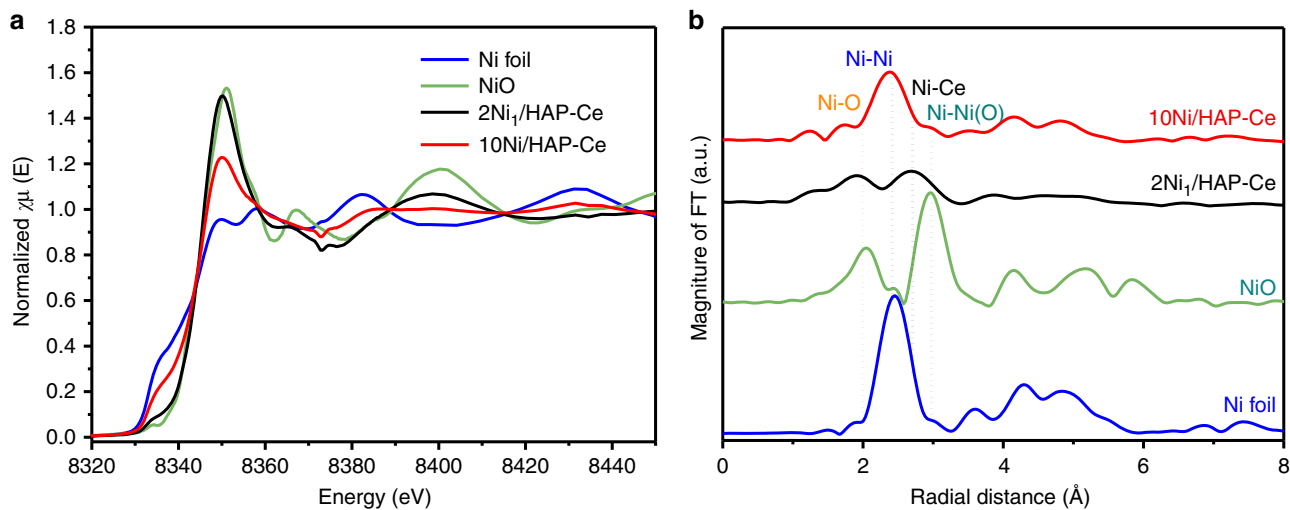


**Fig. 2** X-ray adsorption spectroscopy study of Ni/HAP-Ce catalysts. **a** Ni K-edge XANES spectra of 500 °C reduced HAP-Ce supported Ni catalysts and reference samples, and **b** corresponding phase shift corrected  $k^2$ -weighted Fourier transform

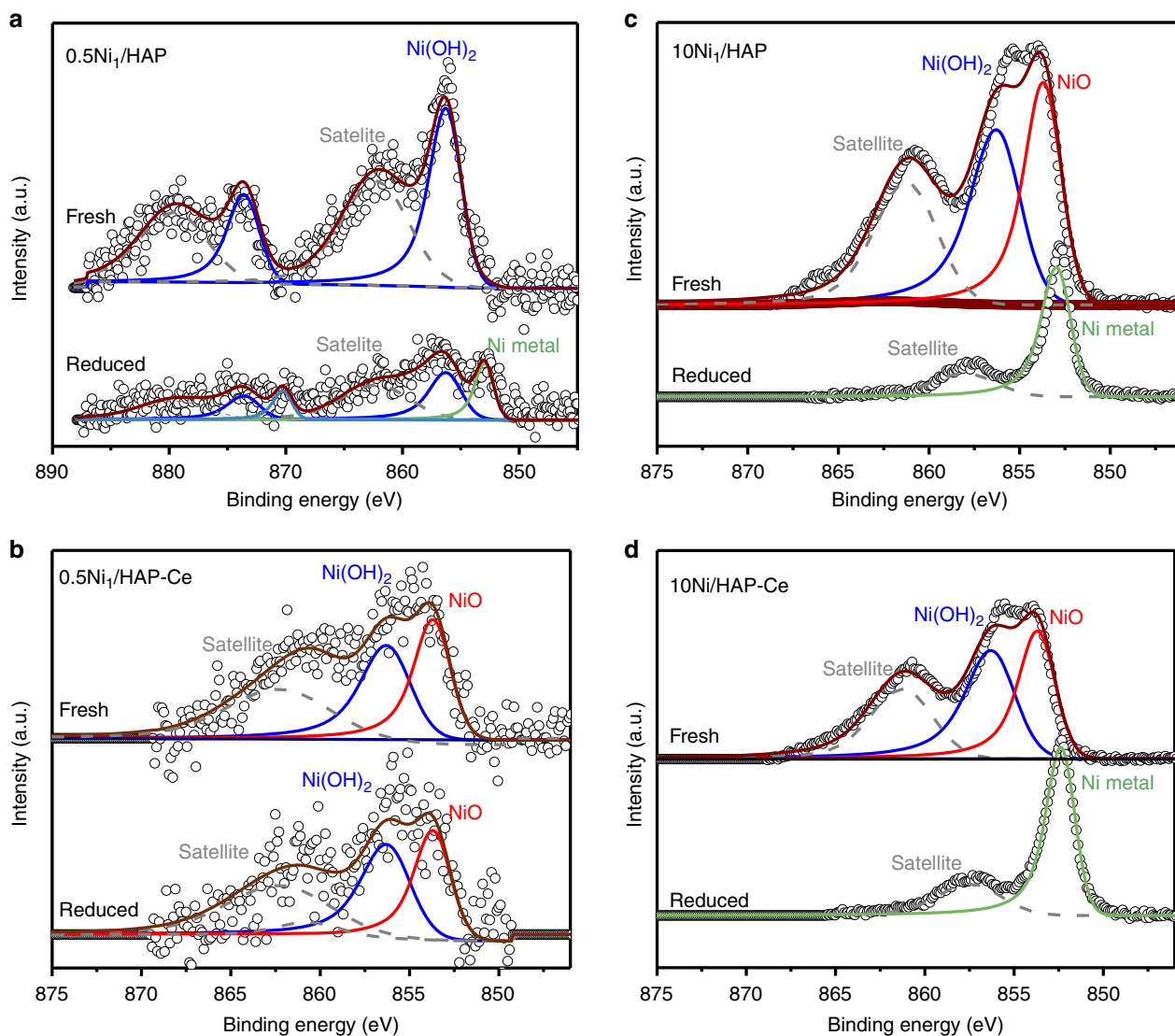


**Fig. 3** In-Situ XPS analysis of Ni/HAP and Ni/HAP-Ce samples. **a** High resolution Ni 2p XP spectra of as-prepared and in situ reduced: 0.5Ni<sub>1</sub>/HAP, **b** 0.5Ni<sub>1</sub>/HAP-Ce, **c** 10Ni<sub>1</sub>/HAP, and **d** 10Ni<sub>1</sub>/HAP-Ce

**Ni SAC electronic structure.** The surface oxidation state of Ni in the preceding as-prepared and reduced samples were studied by X-ray photoelectron spectroscopy (XPS). Since reduced Ni species are prone to ambient oxidation, 500 °C H<sub>2</sub> reduction was performed in situ within a quartz reaction cell prior to direct transfer into the spectrometer without air-exposure. As-prepared 0.5Ni<sub>1</sub>/HAP sample contained only Ni(OH)<sub>2</sub> species at 856.3 eV binding energy (Fig. 3a), consistent with isolated Ni atoms at the hydroxyapatite interface, whereas the as-prepared 10Ni<sub>1</sub>/HAP sample possessed almost equal amounts of Ni(OH)<sub>2</sub> and NiO (853.7 eV), Fig. 3c. In situ reduction of the 10Ni<sub>1</sub>/HAP sample transformed all surface Ni<sup>2+</sup> species to metallic Ni (853.0 eV, Fig. 3c), indicating a relatively weak interaction with the HAP support, and in accordance with the observation of metallic Ni nanocluster/particles by STEM (Supplementary Fig. 7). In contrast, only half of the initial Ni(OH)<sub>2</sub> species in 0.5Ni<sub>1</sub>/HAP underwent reduction to Ni metal (Fig. 3a), suggesting that isolated Ni adatoms experience a stronger support interaction. Figure 3d reveals that Ce doping had negligible impact on the Ni surface chemical state for high loadings, with equimolar Ni(OH)<sub>2</sub> and NiO species present in the as-prepared material, and only metallic Ni observed following in situ

reduction. In contrast, the 0.5Ni<sub>1</sub>/HAP-Ce differed significantly from its undoped counterpart, exhibiting both Ni(OH)<sub>x</sub> and NiO in an almost equimolar ratio in the as-prepared sample, and being entirely resistant to in situ reduction (Fig. 3b). Note that the high binding energy Ni 2p peak in Fig. 3b at 856.3 eV can be assigned to isolated Ni atoms in a distinct Ni(OH)<sub>x</sub> chemical environment, and not from Ni–O–Ni interactions in NiO nanoparticles. Non-local screening of photoexcited core holes only gives rise to peak splitting for the latter when NiO nanostructures exceed ~2.4 nm<sup>38,39</sup>, of which there is no evidence in 0.5Ni<sub>1</sub>/HAP-Ce by either HRTEM (Fig. 1a and Supplementary Figs. 3 and 4) or XRD (Supplementary Fig. 2). The surprising resistance 0.5Ni<sub>1</sub>/HAP-Ce to H<sub>2</sub> reduction was confirmed by temperature-programmed reduction (TPR, Supplementary Fig. 9): high loading 10Ni<sub>1</sub>/HAP and 10Ni<sub>1</sub>/HAP-Ce exhibit almost complete reduction <600 °C associated with Ni metal formation (Supplementary Table. 4); in contrast, 0.5Ni<sub>1</sub>/HAP sample exhibited a weak, broad reduction associated with loss of only ~60% of the initial Ni<sup>2+</sup> species, and 0.5Ni<sub>1</sub>/HAP-Ce showed negligible reducibility. XPS and TPR unambiguously demonstrate that cerium doping of HAP stabilizes atomically dispersed Ni against reduction and sintering.

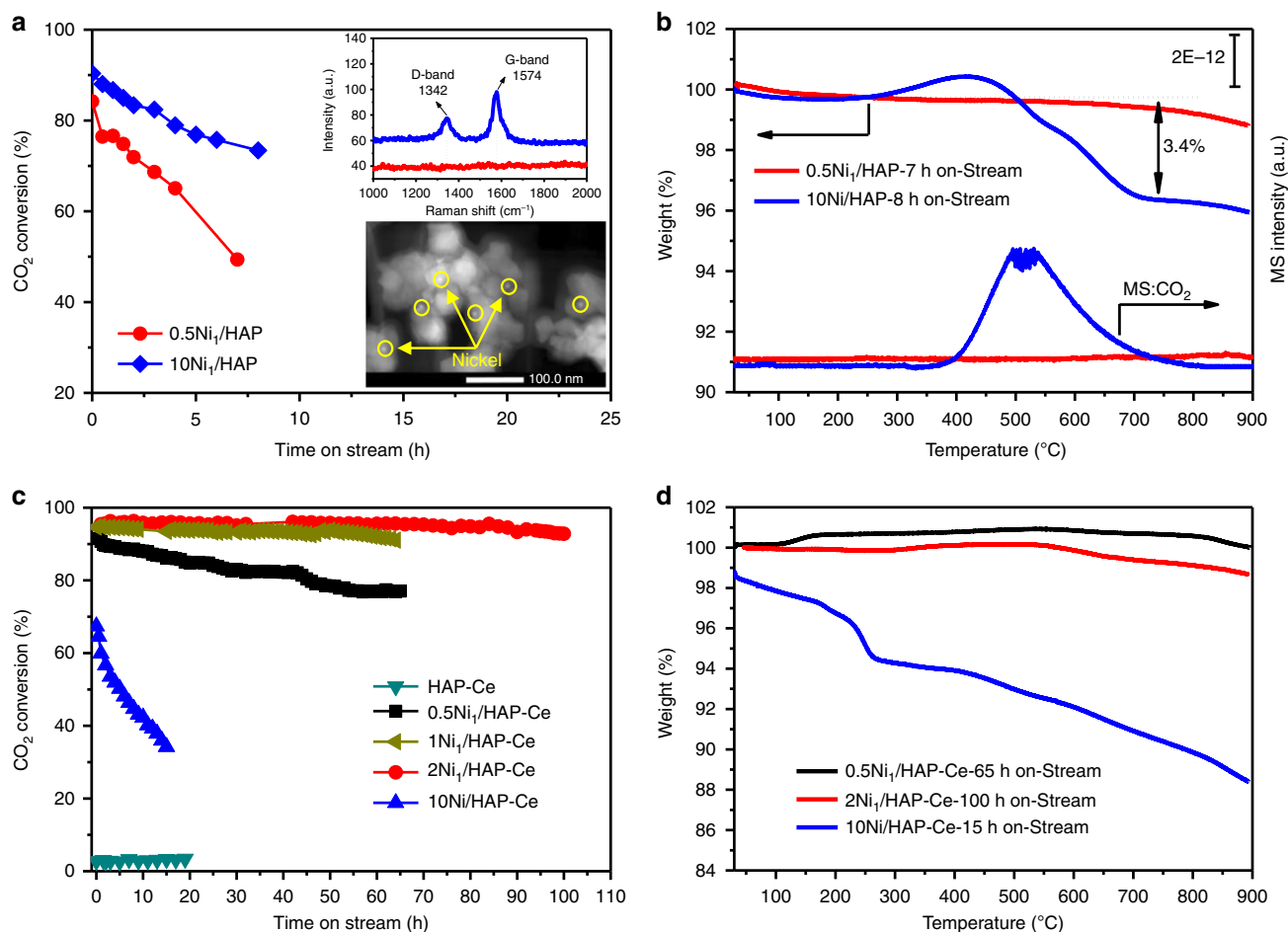


**Fig. 4** DRM performance and carbon deposition analysis over Ni/HAP and Ni/HAP-Ce samples. **a** CO<sub>2</sub> conversion during DRM over HAP and **c** HAP-Ce supported different Ni catalysts. Conditions:  $T = 750\text{ }^{\circ}\text{C}$ ,  $\text{CH}_4/\text{CO}_2/\text{He} = 10/10/30$ , total flow =  $50\text{ mL min}^{-1}$  (GHSV =  $60,000\text{ mL h}^{-1}\text{ g}_{\text{cat}}^{-1}$ ), inset is Raman spectra of spent  $0.5\text{Ni}_1/\text{HAP}$  and  $10\text{Ni}_1/\text{HAP}$  after reaction at  $750\text{ }^{\circ}\text{C}$  and STEM image of  $0.5\text{Ni}_1/\text{HAP}$  after 7 h reaction; **b-d** TGA-MS and TGA profiles of various catalysts after different reaction times on-stream at  $750\text{ }^{\circ}\text{C}$

**Catalytic performance in DRM.** The preceding Ni catalysts were evaluated for DRM using a 20 vol%  $\text{CH}_4 + 20\text{ vol}\%$   $\text{CO}_2$  feed gas (balanced with He) with a gas hourly space velocity (GHSV) of  $60,000\text{ mL g}_{\text{cat}}^{-1}\text{ h}^{-1}$ . All samples were in situ reduced at  $500\text{ }^{\circ}\text{C}$  by 10 vol%  $\text{H}_2/\text{He}$  for 1 h prior to catalytic testing. At  $750\text{ }^{\circ}\text{C}$ , both  $0.5\text{Ni}_1/\text{HAP}$  and  $10\text{Ni}_1/\text{HAP}$  samples underwent rapid deactivation, with  $\text{CO}_2$  conversions decreasing from 84 to 49% and 90 to 73% respectively over 7 h on-stream (Fig. 4a), mirroring corresponding  $\text{CH}_4$  conversions (Supplementary Fig. 10a). However, characterization of post-reaction catalysts indicates that they deactivate by different mechanisms. Temperature-programmed oxidation revealed significant carbon deposition over the deactivated  $10\text{Ni}_1/\text{HAP}$  (Fig. 4b), evidenced by a large weight loss associated with reactively formed  $\text{CO}_2$  desorption between 400 and  $600\text{ }^{\circ}\text{C}$ . The nature of carbon species was analyzed by Raman spectroscopy (Fig. 4a inset). The peak at  $\sim 1328\text{ cm}^{-1}$  (D band) corresponds to  $\text{sp}^3$  carbon atoms at defects and disordered sites<sup>40</sup>, while that  $\sim 1585\text{ cm}^{-1}$  (G band) corresponds to  $\text{sp}^2$  carbon atoms in graphitic rings<sup>41</sup>. In contrast, the  $0.5\text{Ni}_1/\text{HAP}$  sample exhibited negligible carbon deposition (Fig. 4b), albeit large nanoparticles (Fig. 4a inset) emerged from sintering of isolated Ni atoms, apparent from a  $44.55^\circ$  reflection in the post-reaction XRD pattern characteristic of fcc Ni metal (Supplementary Fig. 2d). It is important to note that the  $0.5\text{Ni}_1/\text{HAP}$  SAC shows comparable initial activity to the  $10\text{Ni}_1/\text{HAP}$  despite possessing twenty times less active component. HAP supported

isolated Ni atoms are therefore highly active and resistant to coking, albeit susceptible to sintering during high temperature DRM.

HAADF-STEM (Fig. 1a, b),  $\text{H}_2$ -TPR (Supplementary Fig. 9) and in situ XPS (Fig. 3b) demonstrate that cerium doping of the HAP support stabilizes atomically dispersed Ni to high temperature reduction. This results in a striking performance enhancement for the  $0.5\text{Ni}_1/\text{HAP-Ce}$  catalyst, for which  $\text{CO}_2$  (Fig. 4c) and  $\text{CH}_4$  (Supplementary Fig. 10b) conversions show only a modest decrease from initial  $\sim 90\%$  levels over 65 h reaction. Increasing the Ni loading over the Ce-doped support to 1 wt% and 2 wt% further improved the long-term stability, with such catalysts of  $1\text{Ni}_1/\text{HAP-Ce}$  and  $2\text{Ni}_1/\text{HAP-Ce}$  (mainly composed of single atoms as revealed by Fig. 1b–d, Supplementary Figs. 5 and 6) able to continuously operate at 95%  $\text{CO}_2$  conversion for almost 65 and 100 h, respectively, with a  $\text{H}_2/\text{CO}$  ratio around unity (Supplementary Fig. 10c). These  $\text{Ni}_1/\text{HAP-Ce}$  SACs showed negligible coking (Fig. 4d) and theoretical carbon balance equal to 100% (Supplementary Fig. 10c). By comparison, the  $10\text{Ni}_1/\text{HAP-Ce}$  rapidly deactivated within 15 h on-stream (Fig. 4c) due to severe coking (Fig. 4d) along with a decrease in carbon balance and  $\text{H}_2/\text{CO}$  ratio (Supplementary Fig. 10c). The principal role of Ce therefore appears to be to stabilize atomically dispersed Ni, rather than to suppress carbon deposition. In addition, a control experimental shows that HAP-Ce itself is almost inactive for DRM (Fig. 4c), suggesting that activity

**Table 1** Reaction rate of Ni/HAP and Ni/HAP-Ce catalysts

Catalysts	Ni loading (wt%)	Specific rate (mol. g <sub>Ni</sub> <sup>-1</sup> h <sup>-1</sup> )		TOF (s <sup>-1</sup> )		Temperature (°C)	Note
		CH <sub>4</sub>	CO <sub>2</sub>	CH <sub>4</sub>	CO <sub>2</sub>		
0.5Ni <sub>1</sub> /HAP-Ce	0.5	373.1	729.4	6.1	11.9	750	This work
2Ni <sub>1</sub> /HAP-Ce	2.6	196.4	330.1	5.8	9.8	750	This work
10Ni <sub>1</sub> /HAP-Ce	8.5	88.1	132.4	6.5	9.8	750	This work
Ni@SiO <sub>2</sub>	3.6	1.8	-	0.1	N.A	550	Ref. 58
Ni/SiO <sub>2</sub> @SiO <sub>2</sub>	0.16	144	289	21.2	42.5	800	Ref. 20
Ni/La <sub>2</sub> O <sub>3</sub> -LOC	5.7	8.3	-	7.6	N.A	700	Ref. 59
Ni-Zr/SiO <sub>2</sub>	8.3	0.25	0.35	1.06	1.48	450	Ref. 60
Ni-Si/ZrO <sub>2</sub>	7.8	0.49	0.46	1.38	1.3	450	Ref. 60

predominantly originates from the atomically dispersed Ni. It could be argued that the catalyst reduction temperature is quite low compared with the DRM reaction temperature, even though H<sub>2</sub>-TPR result suggests that our Ni SAC would not be significantly reduced even at 750 °C. To confirm the sinter resistance of our catalysts, the DRM performance of 0.5Ni<sub>1</sub>/HAP-Ce and 2Ni<sub>1</sub>/HAP-Ce pre-reduced at 750 °C was also examined (Supplementary Fig. 11); there was no deterioration relative to 500 °C pre-reduced catalysts.

Recent elegant work by Tang et al.<sup>42</sup> reported a synergy between single-atom Ru<sub>1</sub> and Ni<sub>1</sub> sites resulting in very high activity for DRM even at 600 °C. Significant performance benefits accrued for our catalytic system under identical reaction conditions, even for loadings that do not exclusively give rise to single atoms: the 2 wt% Ni<sub>1</sub>/HAP-Ce catalyst delivered similar activity and superior stability (Supplementary Fig. 11c) without recourse to precious metals.

The faster deactivation of 0.5Ni<sub>1</sub>/HAP-Ce versus 2Ni<sub>1</sub>/HAP-Ce merits consideration. In theory, all active sites within single-atom catalysts are identical and homogeneously distributed. However, in practice the fabrication of a completely homogenous dispersion of single-atom sites is extremely difficult, and there is likely a distribution of coordination numbers and micro-environments<sup>43</sup>. For 0.5Ni<sub>1</sub>/HAP-Ce, we suggest that some single atoms initially present in lower coordination environments (e.g. the edges of HAP crystals) aggregate during reaction to lower their surface energies, resulting in the (albeit very slow) observed deactivation (Fig. 4c and Supplementary Fig. 10b). In contrast, unstable Ni single atoms present in the as-prepared 2Ni<sub>1</sub>/HAP-Ce likely sintered during subsequent reduction to form the small clusters and nanoparticles seen in Fig. 1b. Hence the reduced 2Ni<sub>1</sub>/HAP-Ce catalyst may possess a smaller proportion of unstable single atoms than the reduced 0.5Ni<sub>1</sub>/HAP-Ce catalyst. Note that nanoclusters and nanoparticles also eventually sinter during reaction, but with slower kinetics than isolated atoms (reflecting the higher surface energy and hence instability of the latter). Moreover, even if all isolated Ni atoms in 0.5Ni<sub>1</sub>/HAP-Ce initially occupy low energy surface sites, provided that their interaction with the support is weaker than the cohesive energy between Ni atoms then thermodynamics will always drive sintering for a sufficiently high energy input, at high temperature.

The specific activity of our HAP-Ce supported Ni catalysts was subsequently measured under differential reactor operation at much higher GHSV (528,000–1,056,000 mL h<sup>-1</sup> g<sub>cat</sub><sup>-1</sup>) and low CH<sub>4</sub>/CO<sub>2</sub> conversions (≤25%) to eliminate possible mass- and heat-transfer limitations. Ni/HAP-Ce SACs exhibited much higher specific activity (2–4 times), but an almost identical turnover frequency (TOF), to the nickel nanoclusters and

nanoparticles present for 10Ni<sub>1</sub>/HAP-Ce. The latter suggests a common Ni<sup>2+</sup> active site (likely Ni(OH)<sub>2</sub>), and the former more efficient Ni utilization in the SACs<sup>30,44–46</sup> (a common feature and key advantage of SACs, although less important for earth abundant metal catalysts). Alternatively, the similar TOFs may be a simple coincidence of common energy barriers for different rate-limiting steps over Ni single atoms and nanoparticles. CH<sub>4</sub> activation is generally regarded as rate-limiting for overall DRM<sup>14,47</sup>, with a barrier of ~0.9 eV over Ni(111), representative of the surface of Ni nanoparticles in 2Ni<sub>1</sub>/HAP-Ce, and 10Ni<sub>1</sub>/HAP-Ce<sup>14</sup>. This barrier is very similar to that calculated for activation of the first C–H bond in CH<sub>3</sub>O dehydrogenation over Ni single atoms in 0.5Ni<sub>1</sub>/HAP-Ce (the proposed rate-limiting step, see below). The specific activity of the Ni<sub>1</sub>/HAP-Ce SAC is comparable or superior to that of literature Ni DRM catalysts (Table 1).

**Origin of Ni SAC coke resistance.** DRM usually proceeds according to the following steps: CH<sub>4</sub> decomposes over Ni active sites to form carbon and H<sub>2</sub> (Supplementary Fig. 12) and the resulting carbon is then oxidized by O adatoms liberated by CO<sub>2</sub> dissociation either over the support or at the metal-support interface<sup>13,14,48</sup>. High temperature (>700 °C) coke deposits thus predominantly arise from unoxidized carbon bound to Ni. The coke resistance of Ni SACs may be either intrinsic (i.e. they do not produce carbon from methane) or extrinsic (carbon formed is immediately oxidized by CO<sub>2</sub>); the latter implies superior CO<sub>2</sub> activation. To distinguish between these two mechanisms, carbon deposition in the presence of CH<sub>4</sub> alone was studied at the reaction temperature (750 °C) over 2Ni<sub>1</sub>/HAP-Ce and 10Ni<sub>1</sub>/HAP-Ce catalysts (Fig. 5a, b). In both cases CH<sub>4</sub> decomposition occurred, however the resulting products were different. For 10Ni<sub>1</sub>/HAP-Ce, significant coking was evidenced by a color change (Supplementary Fig. 13a, b) and the large weight loss (8.67%) following TPO post-reaction (Fig. 5c), accompanied by H<sub>2</sub> and ethylene formation (Fig. 5b). In contrast, 2Ni<sub>1</sub>/HAP-Ce produced almost no coke (Supplementary Fig. 13c, d, Fig. 5c), but hydrogen, ethylene. It should be noted that on 2Ni<sub>1</sub>/HAP-Ce much greater C–C coupling occurred, but the H<sub>2</sub> yield was much lower compared with 10Ni<sub>1</sub>/HAP-Ce (Fig. 5d). The Ni SAC therefore favors partial CH<sub>4</sub> dehydrogenation and C–C coupling versus complete decomposition to C (step (4) in Supplementary Fig. 12). This observation is in good agreement with Fe single site catalysts, wherein non-oxidative coupling of CH<sub>4</sub> to ethene and aromatics without attendant coke formation was recently reported<sup>49</sup>. Theoretical calculations also suggest that oxide supported Pt SAC catalysts only efficiently activate the first C–H bond in CH<sub>4</sub>, consistent with our present observations<sup>50</sup>.

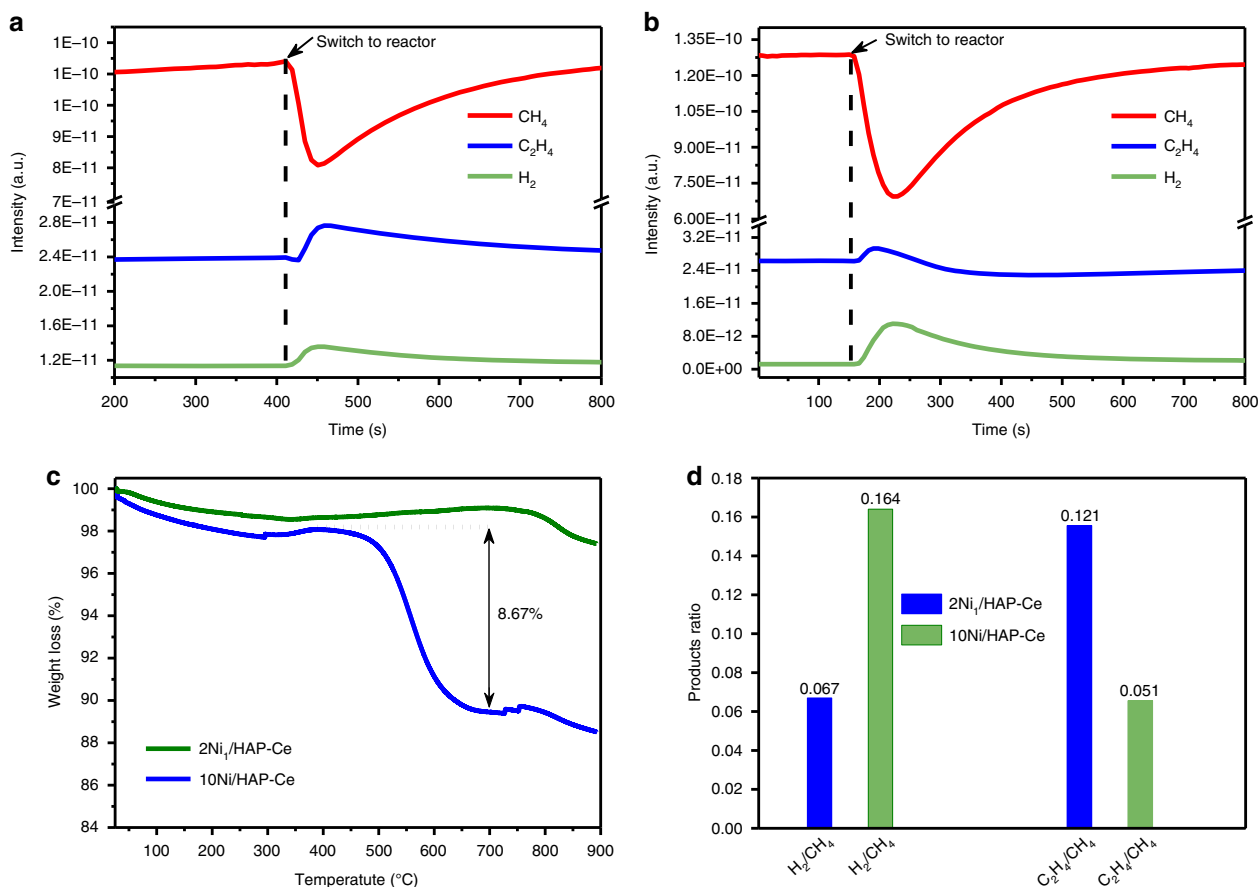


**Fig. 5** CH<sub>4</sub> decomposition and products distribution over Ni/HAP-Ce catalysts. **a** Mass spectrometer signals during CH<sub>4</sub> decomposition at 750 °C of 2Ni<sub>1</sub>/HAP-Ce and **b** 10Ni<sub>1</sub>/HAP-Ce, **c** TGA analysis of both catalysts after 1 h of reaction, and **d** product ratios for non-oxidative methane decomposition. H<sub>2</sub>/CH<sub>4</sub> and C<sub>2</sub>H<sub>4</sub>/CH<sub>4</sub> represent the mass spectrometer product ratio of H<sub>2</sub> and C<sub>2</sub>H<sub>4</sub> relative to the amount of CH<sub>4</sub> reacted

To understand the intrinsic coke resistance of our Ni SACs, underpinned by their selective activation of the first C–H bond, we undertook DFT calculations to investigate the first two steps of CH<sub>4</sub> dissociation over a Ni<sub>1</sub>/CeO<sub>2</sub> surface (Fig. 6a) and subsequent transformation of CH<sub>3</sub> species (Fig. 6b, c). CH<sub>4</sub> adsorption on Ni<sub>1</sub>/CeO<sub>2</sub> (111) is a physisorption process with a small adsorption energy of  $-0.11$  eV, in which the carbon atom of CH<sub>4</sub> is located 2.56 Å above the Ni atom. The first C–H bond cleavage is exothermic by 0.65 eV with an activation barrier of 0.63 eV (TS1). This barrier is considerably lower than that over a Ni(111) surface (0.9 eV)<sup>51</sup>, and hence activation of the first C–H bond in CH<sub>4</sub> is extremely efficient over ceria-bound isolated Ni atoms. The resulting CH<sub>3</sub> species binds atop the Ni atom while the H adatom moves to a neighboring O. The next dehydrogenation step, CH<sub>3</sub> → CH<sub>2</sub> + H, is thermodynamically unfavorable (endothermic by 0.80 eV) with a high activation barrier of 1.54 eV (TS2), and hence CH<sub>3</sub> dissociation is strongly disfavored over Ni<sub>1</sub>/CeO<sub>2</sub>, in excellent agreement with the preceding experiments. In light of the thermodynamic stability of CH<sub>3</sub> to subsequent C–H cleavage over our catalysts, the appearance of CO as a major product in our catalytic system appears paradoxical. However, a recent report of DRM over Ni<sub>4</sub> clusters (which also show good carbon deposition resistance<sup>52</sup>) identified the oxidation of CH<sub>3</sub> to CH<sub>3</sub>O as an alternative route to CO following initial methane activation, as also proposed for Ni<sub>1</sub>-Ru<sub>1</sub>/CeO<sub>2</sub><sup>42</sup>. We therefore considered this alternative route for transforming reactively formed CH<sub>3</sub> to CO without carbon deposition (Fig. 6b, c). Unlike CH<sub>3</sub> dehydrogenation, the oxidation of CH<sub>3</sub> to CH<sub>3</sub>O on Ni<sub>1</sub>/CeO<sub>2</sub> is exothermic with a relatively lower barrier of 0.69 eV.

Subsequent CH<sub>3</sub>O dehydrogenation to CHO is highly exothermic, and the rate-determining step (C–H bond activation in CH<sub>3</sub>O proceeds with a barrier of 0.90 eV) to the final CO product (which is only slightly endothermic by 0.39 eV). The oxidation of CH<sub>3</sub> to CH<sub>3</sub>O is hence plausible as the dominant (indirect) pathway for CH<sub>3</sub> dehydrogenation to CO. Overall, DFT calculations suggest that Ni<sub>1</sub>/CeO<sub>2</sub> should be an active catalyst for CH<sub>4</sub> reforming to CO.

In summary, this work demonstrates that Ni atoms atomically dispersed over HAP are highly resistant to coking during DRM, but prone to on-stream deactivation through sintering. Ce doping of HAP induces strong metal-support interactions which stabilize Ni single atoms towards sintering, and favor selective activation of only the first C–H bond in methane, resulting in a high activity and stability for 100 h DRM with negligible carbon deposition. The excellent performance and stability of Ni single-atom catalysts offers a low-cost route to commercial dry methane reforming. Of broader significance, the findings in this work may provide a new approach for the development of highly coke-resistant Ni-based catalysts.

## Methods

**Chemicals.** Calcium nitrate (99%), cerium nitrate (99%), nickel nitrate (98.5%), ammonium dihydrogen phosphate (99%), and ammonia solution (25 vol% aqueous) were purchased from Sigma-Aldrich and used without pretreatment.

**Synthesis of hydroxyapatite and Ce-substituted HAP.** Stoichiometric hydroxyapatite (Ca:P = 1.67 molar ratio) and Ce substituted hydroxyapatite nanoparticles (5 wt% Ce loading), denoted as HAP and HAP-Ce respectively, were synthesized by co-precipitation of calcium nitrate (Ca(NO<sub>3</sub>)<sub>2</sub>·4H<sub>2</sub>O) and

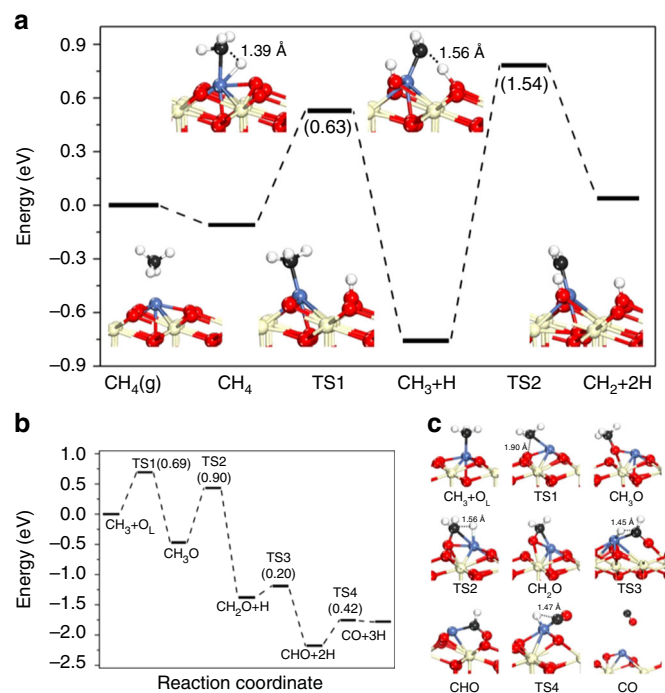


**Fig. 6** DFT calculation of  $\text{CH}_4$  decomposition. **a** Potential energy diagram from DFT calculations of  $\text{CH}_4$  dissociation over  $\text{Ni}_1/\text{CeO}_2$ . **b** Potential energy diagram from DFT calculations of  $\text{CH}_3$  oxidation and  $\text{CH}_3\text{O}$  dehydrogenation, and **c** corresponding geometries over  $\text{Ni}_1/\text{CeO}_2$ . Numbers in parentheses indicate the activation barriers for elementary steps in eV. Optimized structures for reaction intermediates are shown inset (Ce: yellow, Ni: blue, O: red, C: black, H: white)

ammonium dihydrogen phosphate ( $(\text{NH}_4)_2\text{HPO}_4$ ), with or without cerium nitrate ( $\text{Ce}(\text{NO}_3)_2 \cdot 6\text{H}_2\text{O}$ ). Typically, 7.54 g of  $\text{Ca}(\text{NO}_3)_2 \cdot 4\text{H}_2\text{O}$ , and 2.54 g of  $(\text{NH}_4)_2\text{HPO}_4$  were separately dissolved in 80  $\text{cm}^3$  of doubly distilled water, and the pH adjusted to 10.5 with 25 vol% ammonia solution. Ammonium dihydrogen phosphate was added dropwise to the calcium nitrate solution at room temperature, and the resulting milky suspension stirred at 90 °C and 600 rpm for 2 h. The precipitate was rinsed with demineralized water three times prior to drying in air at 80 °C overnight. The dried sample was subsequently calcined at 400 °C (ramp rate 10 °C  $\text{min}^{-1}$ ) in a muffle furnace for 4 h. Ce-substituted hydroxyapatite was synthesized identically except for the addition of the appropriate amount of cerium nitrate to calcium nitrate prior to pH adjustment.

**Ni deposition on HAP and HAP-Ce.** A range of nominal Ni loadings (0.5, 1, 2, and 10 wt%) were deposited on the preceding supports by strong electrostatic adsorption at room temperature. An appropriate amount of nickel nitrate ( $\text{Ni}(\text{NO}_3)_2 \cdot 6\text{H}_2\text{O}$ ) was dissolved in 50 mL deionized water, and the solution pH adjusted to 10 with 25 vol% ammonia solution. The appropriate mass of HAP or HAP-Ce was then added to the nickel nitrate solution, and stirred at 600 rpm for 3 h at room temperature. The resulting impregnated solids were filtered, washed repeatedly with deionized water, and dried at 80 °C overnight prior to calcination at 500 °C (ramp rate 10 °C  $\text{min}^{-1}$ ) for 4 h.

**Characterization.** Actual Ni loadings were determined by inductively coupled plasma spectrometry-atomic emission spectrometry (ICP-AES) on an IRIS Intrepid II XSP instrument (Thermo Electron Corporation). Specific surface areas ( $S_{\text{BET}}$ ) were measured by  $\text{N}_2$  porosimetry on a Micromeritics ASAP 2010 apparatus with adsorption-desorption isotherms recorded at 77 K. Samples were outgassed at 523 K prior to analysis. Surface areas were calculated from the adsorption branch using the Brunauer-Emmett-Teller method, with pore diameters determined from the desorption branch using the BJH method. X-ray diffraction (XRD) patterns were collected on a PW3040/60  $\times$  Pert PRO (PANalytical) diffractometer with  $\text{Cu K}_\alpha$  radiation (0.15432 nm) operating at 40 kV and 40 mA. Patterns were collected between  $2\theta = 10$ –80° at a scan speed of 10°  $\text{min}^{-1}$ .  $\text{CO}_2$  temperature-programmed desorption (TPD) was performed on a Micromeritics AutoChem II 2920 instrument. HAP and HAP-Ce supports were first loaded into a U-shaped quartz reactor, pretreated at 300 °C in He for 0.5 h to remove physisorbed water and surface carbonates, and cooled to 50 °C. Base sites were subsequently saturated with  $\text{CO}_2$  under flowing 10 vol%  $\text{CO}_2$  in He at room temperature. Samples were then purged under He for 30 min prior to heating at 10 °C  $\text{min}^{-1}$  to 900 °C under flowing He

and desorbing  $\text{CO}_2$  detected by TCD. Temperature-programmed reduction ( $\text{H}_2$ -TPR) was also carried out on a Micromeritics AutoChem II 2920 instrument. Samples (100 mg) were placed in a U-shaped quartz reactor and pretreated in flowing Ar (30  $\text{mL min}^{-1}$ ) at 573 K for 30 min, and then ramped to 1073 K at 10 °C  $\text{min}^{-1}$  in flowing 10 vol%  $\text{H}_2/\text{Ar}$  (50  $\text{mL min}^{-1}$ ) and reacted  $\text{H}_2$  detected by TCD.

High-angle annular dark-field scanning transmission electron microscopy (HAADF-STEM) was performed on a JEOL JEM-2100F instrument. Aberration-corrected HAADF-STEM was performed on a JEOL JEM-ARM200F equipped with a CEOS probe corrector with a guaranteed resolution of 0.08 nm. Samples were dispersed by ultrasonication in ethanol, and the resulting solution dropped on to carbon films supported on copper grids.

In situ X-ray photoelectron spectroscopy was performed using a Kratos Axis Ultra-DLD fitted with an electron flood gun neutralizer and a monochromated aluminum X-ray source (1486.8 eV). As-prepared samples were analyzed under UHV conditions ( $<10^{-9}$  Torr) at 40 eV pass energy, and then transferred in vacuo to a quartz high-pressure reaction chamber where they were exposed to a 1 bar static atmosphere of 2 vol%  $\text{H}_2$  in  $\text{N}_2$  and heated to 500 °C at a ramp rate of 10 °C  $\text{min}^{-1}$  for 1 h. Reduced samples were then cooled to room temperature and transferred in vacuo back to the analysis chamber for re-measurement. Spectra were energy referenced to adventitious carbon (284.8 eV), and Shirley background subtracted and fitted using CasaXPS v2.3.19PR1.0. Ni 2p spectra were fitted using a Doniach-Sunjić lineshape convoluted with a Gaussian-Lorentz function.

The X-ray absorption fine structure (XAFS) experiment was performed at the bending magnet beamline BL12B of Spring-8 (8 GeV, 100 mA) belong to National Synchrotron Radiation Research Center, in which the X-ray beam was monochromatized with water-cooled Si (111) double-crystal monochromator and focused with two Rh coated focusing mirrors with the beam size of 2.0 mm in the horizontal direction and 0.5 mm in the vertical direction around sample position. The samples were filled in a phi10 stainless tube for XAFS measurements. All of the samples were measured by both transmission and fluorescence modes at Ni K-edge. The samples were also measured at BL14W1 of the Shanghai Synchrotron Radiation Facility (SSRF) light sources and similar results were obtained. The spectra were analyzed and fitted using an analysis program Demeter<sup>53</sup>. For EXAFS fittings, the crystal structures of Ni foil and NiO are from Materials Project (<https://materialsproject.org>). For  $2\text{Ni}_1/\text{HAP-Ce}$  sample the structure from DFT calculation is used.

**DFT calculations.** All calculations were performed using periodic DFT methods as implemented in the Vienna ab-initio simulation package (VASP)<sup>54,55</sup>. The projector augmented wave (PAW) method was used for the interaction between atomic cores and valence electrons. Valence orbitals of Ce (4f, 5s, 6s, 5p, 5d), Ni (3d, 4s), O (2s, 2p), C (2s, 2p), and H (1s) were described by plane-wave basis sets with cutoff energies of 400 eV, whereas the Brillouin zone was sampled at the  $\Gamma$ -point. Exchange-correlation energies were calculated via the generalized gradient approximation (GGA) with the PBE functional<sup>56</sup>. Spin-polarized DFT + U calculations with a value of  $U_{\text{eff}} = 5.0$  eV for the Ce 4f state were applied to correct the strong electron-correlation properties of  $\text{CeO}_2$ . Convergence criteria for the electronic self-consistent iteration and force were set to  $10^{-4}$  eV and 0.03 eV/Å respectively. For evaluating the energy barriers, transition states and pathways were computed using the climbing image nudged elastic band (CI-NEB) method<sup>57</sup>. The  $\text{CeO}_2$  (111) surface was modeled by  $p(3 \times 3)$  9 atomic layer supercells with the bottom three layers fixed.  $\text{Ni}_1/\text{CeO}_2$  was established by supporting one Ni atom on a  $\text{CeO}_2$  (111) surface (Supplementary Fig. 14). The vacuum gap was set as  $\sim 15$  Å to avoid the interaction between periodic images. Reaction energies and barriers were calculated by  $E_r = E(\text{FS}) - E(\text{IS})$  and  $E_a = E(\text{TS}) - E(\text{IS})$ , where  $E(\text{IS})$ ,  $E(\text{FS})$  and  $E(\text{TS})$  are the energies of the corresponding initial state (IS), final state (FS), and transition state (TS), respectively.

**Catalytic testing.** Catalytic activity tests were performed in a fixed-bed quartz reactor (5 mm i.d.) under atmospheric pressure. Prior to each reaction, 50 mg of catalyst was placed in the reactor tube between quartz wool plugs and reduced in situ at 500 °C or 750 °C under flowing 10 vol%  $\text{H}_2/\text{He}$  (60  $\text{mL min}^{-1}$ ) for 1 h, and then purged with He for 30 min. Dry reforming was then undertaken using a mixture of 20 vol%  $\text{CO}_2 + 20$  vol%  $\text{CH}_4$  in He (50  $\text{mL min}^{-1}$  total flow rate) to generate a gas hourly space velocity (GHSV) of 60,000  $\text{mL g}_{\text{cat}}^{-1} \text{h}^{-1}$ . Specific activities for  $\text{CH}_4$  and  $\text{CO}_2$  conversion were measured at much higher GHSV (using 2.5–5 mg of catalyst, wherein the  $\text{CH}_4$  and  $\text{CO}_2$  conversions were  $<25\%$ ) during the first 60 min of reaction. Reactant and product concentrations were analyzed by an Agilent 6890 online gas chromatograph equipped with a TDX-01 column and a thermal conductivity detector, using He as a carrier gas.  $\text{CH}_4$  and  $\text{CO}_2$  conversions were calculated respectively according to the following Eqs. 1 and 2:

$$C_{\text{CH}_4} = \frac{F_{\text{inlet}} \times [\text{CH}_4] - F_{\text{outlet}} \times [\text{CH}_4]_{\text{outlet}}}{F_{\text{inlet}} \times [\text{CH}_4]_{\text{inlet}}} \quad (1)$$

$$C_{\text{CO}_2} = \frac{F_{\text{inlet}} \times [\text{CO}_2] - F_{\text{outlet}} \times [\text{CO}_2]_{\text{outlet}}}{F_{\text{inlet}} \times [\text{CO}_2]_{\text{inlet}}} \quad (2)$$

Where  $[\text{CH}_4]$  and  $[\text{CO}_2]$  are the respective mole fractions of  $\text{CH}_4$  and  $\text{CO}_2$  in the



feedstream, and  $F_{\text{inlet}}$  and  $F_{\text{outlet}}$  represents the total gas flow rate ( $\text{ml min}^{-1}$ ) of inlet and outlet, respectively. Specific activities for  $\text{CH}_4$  and  $\text{CO}_2$  ( $\text{mol g}_{\text{Ni}}^{-1} \text{h}^{-1}$ ) were calculated from Eqs. 3 and 4:

$$\text{Rate CH}_4 = \frac{n_{\text{CH}_4}}{\text{Weight of catalyst} \times W_{\text{Ni}}} \times 60 \quad (3)$$

$$\text{Rate CO}_2 = \frac{n_{\text{CO}_2}}{\text{Weight of catalyst} \times W_{\text{Ni}}} \times 60 \quad (4)$$

where,

$$n_{\text{CH}_4} = \frac{(F_{\text{inlet}} \times [\text{CH}_4] \times C_{\text{CH}_4})}{(22.4 \times 10^3)} \quad (\text{mol})$$

$$n_{\text{CO}_2} = \frac{(F_{\text{inlet}} \times [\text{CO}_2] \times C_{\text{CO}_2})}{(22.4 \times 10^3)} \quad (\text{mol})$$

and  $F_{\text{inlet}}$  represents the total flow ( $\text{ml min}^{-1}$ ),  $[\text{CH}_4]$ ,  $[\text{CO}_2]$ ,  $C_{\text{CH}_4}$ , and  $C_{\text{CO}_2}$  denote the concentration (vol%) and conversion of  $\text{CH}_4$  and  $\text{CO}_2$ , respectively; and  $W_{\text{Ni}}$  the nickel metal loading (wt%). Turnover frequencies ( $\text{s}^{-1}$ ) were calculated from Eq. 5:

$$\text{TOF} = \frac{n_{\text{CH}_4}}{\text{Weight of catalyst} \times W_{\text{Ni}} \times \frac{\text{Dispersion}}{58.7} \times 60} \quad (5)$$

assuming a dispersion of 100% for  $0.5\text{Ni}_1/\text{HAP-Ce}$ , and values calculated for  $2\text{Ni}_1/\text{HAP-Ce}$  and  $10\text{Ni}_1/\text{HAP-Ce}$  according to the following Eq. 6.

$$D(\%) = \frac{1.0092}{d_{\text{V}_A}} \quad (6)$$

where  $d_{\text{V}_A}$  represent the mean diameter of nickel particles (nm).

## Data availability

The data that support the findings of this study are available within the paper and its Supplementary Information, and all data are available from the authors on reasonable request.

Received: 18 April 2019; Accepted: 1 October 2019;

Published online: 15 November 2019

## References

- Bradford, M. C. J. & Vannice, M. A.  $\text{CO}_2$  reforming of  $\text{CH}_4$ . *Catal. Rev. Sci. Eng.* **41**, 1–42 (1999).
- Pakhare, D. & Spivey, J. A review of dry ( $\text{CO}_2$ ) reforming of methane over noble metal catalysts. *Chem. Soc. Rev.* **43**, 7813–7837 (2014).
- Shi, L. et al. An introduction of  $\text{CO}_2$  conversion by dry reforming with methane and new route of low-temperature methanol synthesis. *Acc. Chem. Res.* **46**, 1838–1847 (2013).
- Zhong, L. et al. Cobalt carbide nanoprisms for direct production of lower olefins from syngas. *Nature* **538**, 84 (2016).
- Cheng, K. et al. Direct and highly selective conversion of synthesis gas into lower olefins: design of a bifunctional catalyst combining methanol synthesis and carbon–carbon coupling. *Angew. Chem. Int. Ed.* **55**, 4725–4728 (2016).
- Gao, P. et al. Direct conversion of  $\text{CO}_2$  into liquid fuels with high selectivity over a bifunctional catalyst. *Nat. Chem.* **9**, 1019–1024 (2017).
- Hu, Y. H.  $\text{CO}_2$  Conversion and Utilization Chunshan Song, Anne F. Gaffney, and Kaoru Fujimoto, Editors. American Chemical Society: Washington, D.C. 2002. xiii + 428 pp. *Energy Fuels* **16**, 1329–1329 (2002).
- Sun, Z., Ma, T., Tao, H., Fan, Q. & Han, B. Fundamentals and challenges of electrochemical  $\text{CO}_2$  reduction using two-dimensional. *Mater. Chem.* **3**, 560–587 (2017).
- He, M., Sun, Y. & Han, B. Green carbon science: scientific basis for integrating carbon resource processing, utilization, and recycling. *Angew. Chem. Int. Ed.* **52**, 9620–9633 (2013).
- Ashcroft, A. T., Cheetham, A. K., Green, M. L. H. & Vernon, P. D. F. Partial oxidation of methane to synthesis gas using carbon dioxide. *Nature* **352**, 225–226 (1991).
- Akri, M. et al. Development of nickel supported La and Ce-natural illite clay for autothermal dry reforming of methane: Toward a better resistance to deactivation. *Appl. Catal. B* **205**, 519–531 (2017).
- Lavoie, J.-M. Review on dry reforming of methane, a potentially more environmentally-friendly approach to the increasing natural gas exploitation. *Front. Chem.* **2**, 81 (2014).
- Foppa, L. et al. Contrasting the role of  $\text{Ni}/\text{Al}_2\text{O}_3$  interfaces in water–gas shift and dry reforming of methane. *J. Am. Chem. Soc.* **139**, 17128–17139 (2017).
- Liu, Z. et al. Dry reforming of methane on a highly-active Ni-CeO<sub>2</sub> catalyst: effects of metal-support interactions on C-H bond breaking. *Angew. Chem. Int. Ed.* **55**, 7455–7459 (2016).
- Buelens, L. C., Galvita, V. V., Poelman, H., Detavernier, C. & Marin, G. B. Super-dry reforming of methane intensifies  $\text{CO}_2$  utilization via Le Chatelier's principle. *Science* **354**, 449 (2016).
- Akri, M., Chafik, T., Granger, P., Ayrault, P. & Batiot-Dupeyrat, C. Novel nickel promoted illite clay based catalyst for autothermal dry reforming of methane. *Fuel* **178**, 139–147 (2016).
- Abdullah, B., Abd Ghani, N. A. & Vo, D.-V. N. Recent advances in dry reforming of methane over Ni-based catalysts. *J. Clean. Prod.* **162**, 170–185 (2017).
- Pawar, V., Ray, D., Subrahmanyam, C. & Janardhanan, V. M. Study of short-term catalyst deactivation due to carbon deposition during biogas dry reforming on supported Ni catalyst. *Energy Fuels* **29**, 8047–8052 (2015).
- Theofanidis, S. A., Galvita, V. V., Poelman, H. & Marin, G. B. Enhanced carbon-resistant dry reforming Fe-Ni catalyst: role of Fe. *ACS Catal.* **5**, 3028–3039 (2015).
- Han, J. W., Park, J. S., Choi, M. S. & Lee, H. Uncoupling the size and support effects of Ni catalysts for dry reforming of methane. *Appl. Catal. B* **203**, 625–632 (2017).
- Lercher, J. A., Bitter, J. H., Hally, W., Niessen, W. & Seshan, K. *Studies in Surface Science and Catalysis*, Vol. 101, 463–472 (Elsevier, 1996).
- Tang, S. et al.  $\text{CO}_2$  reforming of methane to synthesis gas over sol-gel-made Ni/ $\gamma\text{-Al}_2\text{O}_3$  catalysts from organometallic precursors. *J. Catal.* **194**, 424–430 (2000).
- Qiao, B. et al. Single-atom catalysis of CO oxidation using  $\text{Pt}_1/\text{FeO}_x$ . *Nat. Chem.* **3**, 634–641 (2011).
- Flytzani-Stephanopoulos, M. & Gates, B. C. Atomically dispersed supported metal catalysts. *Annu. Rev. Chem. Biomol. Eng.* **3**, 545–574 (2012).
- Wang, A., Li, J. & Zhang, T. Heterogeneous single-atom catalysis. *Nat. Rev. Chem.* **2**, 65–81 (2018).
- Yang, H. B. et al. Atomically dispersed Ni(i) as the active site for electrochemical  $\text{CO}_2$  reduction. *Nat. Energy* **3**, 140–147 (2018).
- Lin, L. et al. Low-temperature hydrogen production from water and methanol using Pt/ $\alpha\text{-MoC}$  catalysts. *Nature* **544**, 80 (2017).
- Lin, L. et al. A highly CO-tolerant atomically dispersed Pt catalyst for chemoselective hydrogenation. *Nat. Nanotechnol.* **14**, 354–361 (2019).
- Zhang, Z. et al. Thermally stable single atom Pt/m- $\text{Al}_2\text{O}_3$  for selective hydrogenation and CO oxidation. *Nat. Commun.* **8**, 16100 (2017).
- Qiao, B. et al. Ultrastable single-atom gold catalysts with strong covalent metal-support interaction (CMSI). *Nano Res.* **8**, 2913–2924 (2015).
- Jones, J. et al. Thermally stable single-atom platinum-on-ceria catalysts via atom trapping. *Science* **353**, 150–154 (2016).
- Lang, R. et al. Non defect-stabilized thermally stable single-atom catalyst. *Nat. Commun.* **10**, 234 (2019).
- Ren, G.-Q. et al. Exceptional antisintering gold nanocatalyst for diesel exhaust oxidation. *Nano. Lett.* **18**, 6489–6493 (2018).
- Xie, P. et al. Nanoceria-supported single-atom platinum catalysts for direct methane conversion. *ACS Catal.* **8**, 4044–4048 (2018).
- Tang, H. et al. Strong metal–support interactions between gold nanoparticles and nonoxides. *J. Am. Chem. Soc.* **138**, 56–59 (2016).
- Li, T. et al. Maximizing the number of interfacial sites in single-atom catalysts for the highly selective, solvent-free oxidation of primary alcohols. *Angew. Chem. Int. Ed. Engl.* **57**, 7795–7799 (2018).
- DeRita, L. et al. Catalyst architecture for stable single atom dispersion enables site-specific spectroscopic and reactivity measurements of CO adsorbed to Pt atoms, oxidized Pt clusters, and metallic Pt clusters on  $\text{TiO}_2$ . *J. Am. Chem. Soc.* **139**, 14150–14165 (2017).
- Alders, D., Voogt, F. C., Hibma, T. & Sawatzky, G. A. Nonlocal screening effects in 2p x-ray photoemission spectroscopy of NiO (100). *Phys. Rev. B* **54**, 7716–7719 (1996).
- Yamauchi, R. et al. Layer matching epitaxy of NiO thin films on atomically stepped sapphire (0001) substrates. *Sci. Rep.* **5**, 14385 (2015).
- Xie, Z. et al. Dry reforming of methane over CeO<sub>2</sub>-supported Pt-Co catalysts with enhanced activity. *Appl. Catal. B* **236**, 280–293 (2018).
- Bokobza, L., Bruneel, J.-L. & Couzi, M. Raman spectroscopy as a tool for the analysis of carbon-based materials (highly oriented pyrolytic graphite, multilayer graphene and multiwall carbon nanotubes) and of some of their elastomeric composites. *Vib. Spectrosc.* **74**, 57–63 (2014).
- Tang, Y. et al. Synergy of single-atom Ni<sub>1</sub> and Ru<sub>1</sub> sites on CeO<sub>2</sub> for dry reforming of CH<sub>4</sub>. *J. Am. Chem. Soc.* **141**, 7283–7293 (2019).
- Liu, W. et al. Discriminating catalytically active FeNx species of atomically dispersed Fe–N–C catalyst for selective oxidation of the C–H bond. *J. Am. Chem. Soc.* **139**, 10790–10798 (2017).
- Qiao, B. et al. Highly efficient catalysis of preferential oxidation of CO in H<sub>2</sub>-rich stream by gold single-atom catalysts. *ACS Catal.* **5**, 6249–6254 (2015).
- Cao, L. et al. Atomically dispersed iron hydroxide anchored on Pt for preferential oxidation of CO in H<sub>2</sub>. *Nature* **565**, 631–635 (2019).
- Yan, H. et al. Single-atom Pd<sub>1</sub>/graphene catalyst achieved by atomic layer deposition: remarkable performance in selective hydrogenation of 1,3-butadiene. *J. Am. Chem. Soc.* **137**, 10484–10487 (2015).

47. Wei, J. & Iglesia, E. Mechanism and site requirements for activation and chemical conversion of methane on supported Pt clusters and turnover rate comparisons among noble metals. *J. Phys. Chem. B* **108**, 4094–4103 (2004).
48. Bradford, M. C. J. & Albert Vannice, M. The role of metal–support interactions in CO<sub>2</sub> reforming of CH<sub>4</sub>. *Catal. Today* **50**, 87–96 (1999).
49. Guo, X. et al. Direct, nonoxidative conversion of methane to ethylene, aromatics, and hydrogen. *Science* **344**, 616–619 (2014).
50. Zhang, C. J. & Hu, P. The possibility of single C–H bond activation in CH<sub>4</sub> on a MoO<sub>3</sub>-supported Pt catalyst: a density functional theory study. *J. Chem. Phys.* **116**, 4281–4285 (2002).
51. Zhu, Y.-A., Chen, D., Zhou, X.-G. & Yuan, W.-K. DFT studies of dry reforming of methane on Ni catalyst. *Catal. Today* **148**, 260–267 (2009).
52. Zuo, Z. et al. Dry reforming of methane on single-site Ni/MgO catalysts: importance of site confinement. *ACS Catal.* **8**, 9821–9835 (2018).
53. Ravel, B. & Newville, M. ATHENA, ARTEMIS, HEPHAESTUS: data analysis for X-ray absorption spectroscopy using IFEFFIT. *J. Synchrotron Radiat.* **12**, 537–541 (2005).
54. Kresse, G. & Furthmüller, J. Efficiency of ab-initio total energy calculations for metals and semiconductors using a plane-wave basis set. *Comput. Mater. Sci.* **6**, 15–50 (1996).
55. Kresse, G. & Furthmüller, J. Efficient iterative schemes for ab initio total-energy calculations using a plane-wave basis set. *Phys. Rev. B Condens. Mater.* **54**, 11169–11186 (1996).
56. Perdew, J. P., Burke, K. & Ernzerhof, M. Generalized gradient approximation made simple. *Phys. Rev. Lett.* **77**, 3865–3868 (1996).
57. Henkelman, G., Uberuaga, B. P. & Jónsson, H. A climbing image nudged elastic band method for finding saddle points and minimum energy paths. *J. Chem. Phys.* **113**, 9901–9904 (2000).
58. Wang, F. et al. CO<sub>2</sub> reforming with methane over small-sized Ni@SiO<sub>2</sub> catalysts with unique features of sintering-free and low carbon. *Appl. Catal. B* **235**, 26–35 (2018).
59. Li, X. et al. Dry reforming of methane over Ni/La<sub>2</sub>O<sub>3</sub> nanorod catalysts with stabilized Ni nanoparticles. *Appl. Catal. B Environ.* **202**, 683–694 (2017).
60. Wang, Y. et al. Low-temperature catalytic CO<sub>2</sub> dry reforming of methane on Ni-Si/ZrO<sub>2</sub> catalyst. *ACS Catal.* **8**, 6495–6506 (2018).

## Acknowledgements

This paper is dedicated to the 70th anniversary of the Dalian Institute of Chemical Physics, Chinese Academy of Sciences. This work was supported by the National Key R&D Program of China (2016YFA0202801, 2017YFA0700104, and 2017YFA0402800); National Natural Science Foundation of China (21776270, 21606222, and 51761165012), Strategic Priority Research Program of the Chinese Academy of Sciences (XDDB17020000), DNL Cooperation Fund, CAS (DNL180403) and LiaoNing Revitalization Talents Program (XLYC1807068). DFT calculations were supported by Beijing Natural Science Foundation (2184097). J.L. thanks National Program for Thousand Young Talents of China.

## Author contributions

M.A. performed the catalyst preparation, catalytic tests, and routine characterizations. S.Z. performed the DFT calculations. K.Z., W.X., and J.L. performed AC HAADF-STEM measurements. Y.S., X.P., X.L., and Lin.L. performed HRTEM measurements. A.F.L., M.A.I., and K.W. conducted in situ XPS measurements and data analysis. Y.R., Y.C., Lei.L., H.I., and Y.L. performed the EXAFS measurement and corresponding data analysis. W.W., Y.G., and Y.P. performed the MS detection. B.Q., A.W., X.W., and T.Z. designed the study, analyzed the data, and co-wrote the paper with input from A.F.L. All the authors discussed the results and commented on the manuscript and contributed to writing the STEM sections.

## Competing interests

The authors declare no competing interests.

## Additional information

**Supplementary information** is available for this paper at <https://doi.org/10.1038/s41467-019-12843-w>.

**Correspondence** and requests for materials should be addressed to B.Q. or T.Z.

**Peer review information** *Nature Communications* thank Changwei Hu and other anonymous reviewers for their contributions to the peer review of this work. Peer review reports are available.

**Reprints and permission information** is available at <http://www.nature.com/reprints>

**Publisher's note** Springer Nature remains neutral with regard to jurisdictional claims in published maps and institutional affiliations.



**Open Access** This article is licensed under a Creative Commons Attribution 4.0 International License, which permits use, sharing, adaptation, distribution and reproduction in any medium or format, as long as you give appropriate credit to the original author(s) and the source, provide a link to the Creative Commons license, and indicate if changes were made. The images or other third party material in this article are included in the article's Creative Commons license, unless indicated otherwise in a credit line to the material. If material is not included in the article's Creative Commons license and your intended use is not permitted by statutory regulation or exceeds the permitted use, you will need to obtain permission directly from the copyright holder. To view a copy of this license, visit <http://creativecommons.org/licenses/by/4.0/>.

© The Author(s) 2019